Modeling and Experimental Validation of the Intrinsic SNR in Spin Qubit Gate-Based Readout and Its Impacts on Readout Electronics

Prabowo, Bagas; Dijkema, Jurgen; Xue, Xiao; Sebastiano, Fabio; Vandersypen, Lieven M.K.; Babaie, Masoud

Modeling and Experimental Validation of the Intrinsic SNR in Spin Qubit Gate-Based Readout and Its Impacts on Readout Electronics

BAGAS PRABOWO[1,2] (Student Member, IEEE), **JURGEN DIJKEMA[2,3]**,
XIAO XUE[2,3], **FABIO SEBASTIANO[1,2]** (Senior Member, IEEE),
LIEVEN M. K. VANDERSYPEN[2,3],
AND MASOUD BABAIE[2,4] (Senior Member, IEEE)

[1]Department of Quantum and Computer Engineering, Delft University of Technology, 2600 Delft, The Netherlands
[2]QuTech, Delft University of Technology, 2600 Delft, The Netherlands
[3]Kavli Institute of Nanoscience, Delft University of Technology, 2600 Delft, The Netherlands
[4]Department of Microelectronics, Delft University of Technology, 2600 Delft, The Netherlands

Corresponding author: Bagas Prabowo (e-mail: b.prabowo@tudelft.nl).

ABSTRACT In semiconductor spin quantum bits (qubits), the radio-frequency (RF) gate-based readout is a promising solution for future large-scale integration, as it allows for a fast, frequency-multiplexed readout architecture, enabling multiple qubits to be read out simultaneously. This article introduces a theoretical framework to evaluate the effect of various parameters, such as the readout probe power, readout chain's noise performance, and integration time on the intrinsic readout signal-to-noise ratio, and thus readout fidelity of RF gate-based readout systems. By analyzing the underlying physics of spin qubits during readout, this work proposes a qubit readout model that takes into account the qubit's quantum mechanical properties, providing a way to evaluate the tradeoffs among the aforementioned parameters. The validity of the proposed model is evaluated by comparing the simulation and experimental results. The proposed analytical approach, the developed model, and the experimental results enable designers to optimize the entire readout chain effectively, thus leading to a faster, lower power readout system with integrated cryogenic electronics.

INDEX TERMS Cryo-CMOS, cryogenic, double quantum dot (DQD), electronics, noise temperature, quantum capacitance, radio-frequency (RF) gate-based readout, readout fidelity, readout signal-to-noise ratio (SNR), spin qubits.

I. INTRODUCTION

Performing practical, fault-tolerant quantum algorithms with quantum error correction (QEC) will require thousands of quantum bits (qubits) in a quantum computer (QC) to be manipulated and read out simultaneously [1]. In the case of a semiconductor spin qubit QC, the QEC cycle must be able to read, decode the error, and apply the correction to the data qubits far faster than the qubit's dephasing time (T_2^*) [2]. Because of the short T_2^* of $\sim$20 μs [3], [4], [5], it is essential to reduce the readout, decode, and gate operation time to be below the sub-μs range for the QEC cycle time to be significantly faster than the dephasing time.

In the case of reducing the readout time of the quantum processor, the choice in the readout technique plays a crucial role. With the requirement of reading thousands of qubits in the future, the choice of the readout architecture must be fast and scalable. One of the most promising readout techniques pursued currently for semiconductor spin qubits is the gate-based readout technique, as it allows the readout architecture to adopt frequency division multiplex access (FDMA) feature to enable the simultaneous readout of multiple qubits by a single receiver (RX) [6], [7], [8].

A simplified model of a gate-based readout architecture is illustrated in Fig. 1(a), where port-1 and port-2 indicate the input and output ports of the readout system, respectively. In principle, the readout architecture has a state-dependent transmission (or reflection) behavior dependent on the qubit's state. To read the qubit's state, the system is
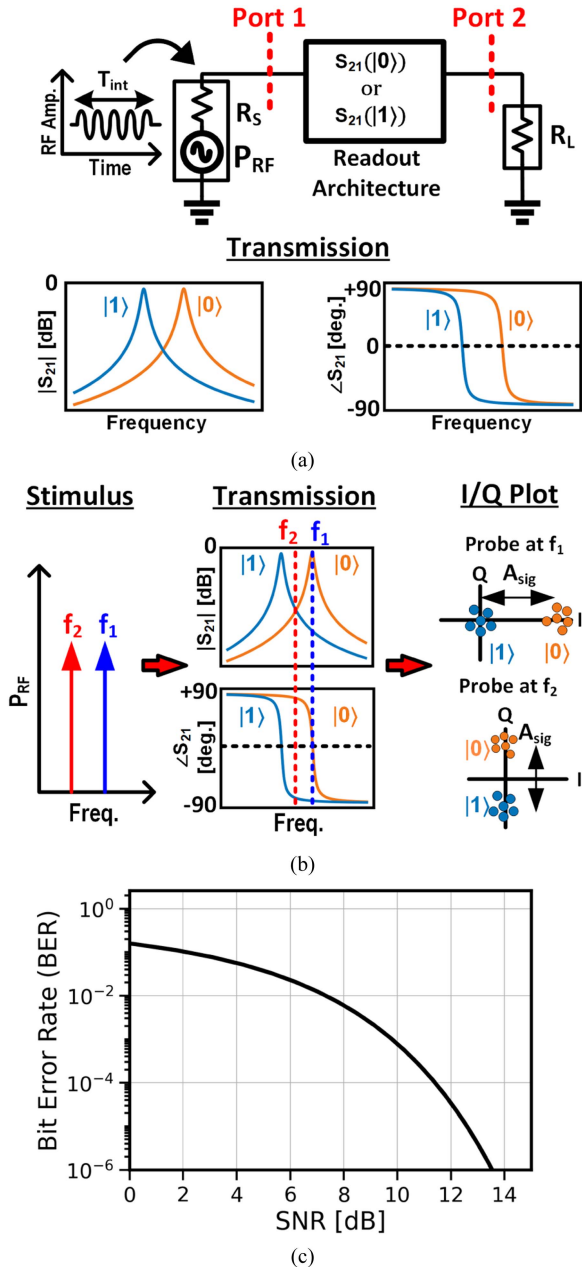
FIGURE 1. (a) Prototype of a readout architecture. (b) Corresponding probe tones, transmission responses of the sample, and constellation diagrams when the system is probed at f_1 and f_2. (c) BER versus SNR plot.

probed with a radio-frequency (RF) tone from port-1 with a certain time duration, T_{int}. Depending on the frequency of the stimulus tone, the readout tone observed at port-2 exhibits a change in amplitude or phase, providing information about the qubit's state. As an example, Fig. 1(b) illustrates the read-out system's response when probed at f_1 and f_2. When the system is probed at the resonance frequency of the $|0\rangle$ state (f_1), the readout signal observed at port-2 resembles a binary amplitude shift keying signal (BASK), due to the attenuated $|1\rangle$ response. On the other hand, when the system is probed at a frequency precisely between the $|0\rangle$ or $|1\rangle$ response (f_2),

the output signal at port-2 resembles a binary phase shift keying signal (BPSK), where the $|0\rangle$ and $|1\rangle$ responses differ by 180°. Regardless of how the output signal is modulated, the readout signal can be denoted as A_{sig} in the constellation diagram, which describes the separation between the two states' responses.

In general, the readout signal (i.e., A_{sig}) must be large enough to accommodate the thermal noise contributed by the environment and the additional noise of the subsequent readout electronics, which is responsible for amplifying and downconverting the readout signal. To quantify the effect of the noise on the readout signal, the readout signal-to-noise ratio (SNR) must be calculated, which depends on both the power of the readout signal (P_{Sig}) and the total noise observed at the input of the readout electronics (P_N). Mathematically, P_{Sig} is related to A_{sig} by

$$P_{Sig} = \frac{|A_{sig}|^2}{R_L} = P_{RF} \left| \left(S_{21,|0\rangle}(\omega_r) - S_{21,|1\rangle}(\omega_r) \right) \right|^2 \quad (1)$$

where P_{RF} is the power delivered by the RF source to the input port of the system (i.e., port-1), ω_r is the readout angular frequency, and $|(S_{21,|0\rangle}(\omega_r) - S_{21,|1\rangle}(\omega_r))|^2$ is the *state-separation factor*, which depends on the S_{21} behavior of the system when it is in the $|0\rangle$ or $|1\rangle$ state. The noise power, P_N, on the other hand, can be expressed as N_0/T_{int}, where N_0 is the noise power spectral density, which includes the noise of the electronics referred to port-2, and T_{int} is the integration time. By defining the SNR as P_{Sig}/P_N, the readout SNR can be expressed as

$$\text{SNR} = \frac{P_{RF}}{N_0/T_{int}} \times \left| \left(S_{21,|0\rangle}(\omega_r) - S_{21,|1\rangle}(\omega_r) \right) \right|^2. \quad (2)$$

However, the quality of the readout acquisition is commonly characterized using metrics, such as the bit error rate (BER) (equivalently, the readout infidelity, $1 - F$) rather than the SNR. The relationship between the SNR in (2) with the BER can be described as

$$\text{BER} = Q\left(\sqrt{\text{SNR}} \right) \quad (3)$$

where $Q(\cdot)$ is the tail distribution function of the standard normal distribution. Based on (3), the resulting BER for a given SNR performance is shown in Fig. 1(c). In fault-tolerant QC with QEC, a target BER of 10^{-4} is often desired, which corresponds to an SNR requirement of 11.5 dB.

The target SNR of 11.5 dB can be achieved in numerous ways, based on (2). Given a readout system with a certain state-separation factor, one could choose an arbitrary P_{RF}, N_0, and a T_{int} that complies with the desired SNR. However, in the context of QEC, T_{int} is commonly fixed based on the QEC requirements. Thus, only P_{RF} and N_0 are left to be optimized to achieve the required SNR. By maximizing P_{RF}, N_0 can be made larger while still achieving the desired SNR. The larger tolerable N_0 benefits the readout electronics by allowing them to be designed at a lower power. With the limited power budget available at the cryogenic level of the dilution refrigerator, this approach enables better integration
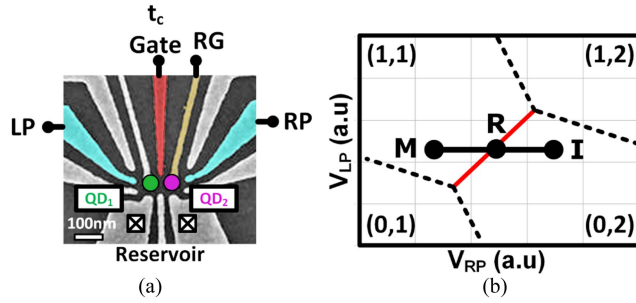
FIGURE 2. (a) False-colored image of a DQD. The QD locations are indicated by colored circles. The RG is connected to a resonator, which is used to probe the system. (b) Sketch of the charge stability diagram of the DQD. The red solid lines indicate the interdot regime. Initialization, manipulation, and readout regimes are labeled correspondingly.

FIGURE 3. (a) Energy levels of a two-electron system, resulting in singlet and triplet configurations. ΔE_z denotes the Zeeman splitting energy while E_{ST} indicates the energy difference between S and T_0 states. (b) Corresponding electron occupation in the two lowest orbitals.

of cryogenic electronics suitable for future large-scale integration.

Experimental observations; however, have shown that increasing P_{RF} does not necessarily improve the readout SNR [9], [10], [11]. Theoretically, (2) shows a boundless tradeoff between P_{RF} and N_0, where a large P_{RF} allows N_0 to be increased proportionally for a given target SNR, T_{int}, and state-separation factor, contradicting experimental observation. Thus, the limit in which N_0 can be relaxed as P_{RF} increases remains unclear. In this article, we investigate the validity of (2) by first constructing a qubit model that considers its quantum mechanical behavior during readout. The proposed model is used to simulate the behavior of a readout system to investigate the validity of (2) and the limitations of the tradeoffs between P_{RF} and N_0. To confirm the behavior shown by our proposed model, the simulated results are compared with experimental results.

The rest of this article is organized as follows. Section II first discusses the behavior of the qubits during readout and how they can be modeled. Section III presents the simulation results of the readout system when the proposed qubit model is considered. Section IV compares the simulated results with experimental results, verifying the validity of the model. Upon experimental verification, Section V discusses the limitations of the proposed model and the impact of the tradeoffs between P_{RF} and N_0 on the readout architecture. Finally, Section VI concludes this article.

II. SPIN QUBIT READOUT THEORY
A. DOUBLE QUANTUM DOT (DQD)
The DQD is the basic building block of a semiconductor spin qubit. Similar to a transistor, the DQD is composed of several plunger gates to control the potential landscape of the device to trap electrons in each respective quantum dot (QD), as indicated by the green and purple circles in Fig. 2(a). By varying the left- (V_{LP}) and right-hand side (V_{RP}) plunger gate voltages, individual electrons can be loaded in and out of each QD site from the electron reservoir, as indicated by the crossed boxes in Fig. 2(a). The tunnel coupling (t_c) gate shown in the figure controls the tunnel coupling interaction
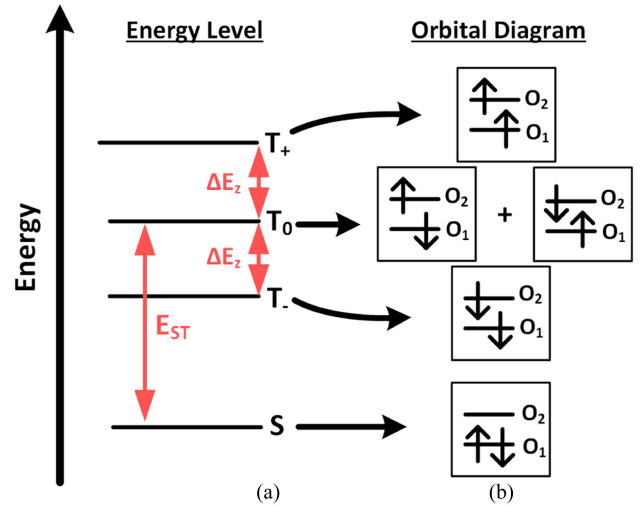
between the two QDs and plays an essential role in tuning the device for readout.

The DQD is typically characterized by the charge stability diagram, as shown in Fig. 2(b). The number (N_L, N_R) indicates the number of electrons in the left- and right-hand side QD, respectively. The dotted black lines in the diagram indicate the plunger gate voltages at which the electrons from the QD can be loaded or unloaded to the reservoir. For quantum computation with spin qubits, initialization can take place in the (0,2) regime, marked as "I" in Fig. 2(b). Once initialized, qubit manipulation can be executed in the (1,1) charge regime at point "M," where the electron spin in the left-hand side QD can be manipulated independently while keeping the right-hand side QD unaffected such that it can be used as a reference for readout [5]. To read the spin state of the left-hand side QD, the DQD is biased at the interdot regime [highlighted in red in Fig. 2(b)]. Depending on the final spin state to which the DQD collapses, the electron may oscillate or stay in each respective dot in response to an RF tone applied at the readout gate (RG), leading to a state-dependent behavior, as discussed in detail below.

The spin states of the DQD and their energy levels in the (1,1)–(0,2) charge regimes must be evaluated to understand how the state-dependent behavior is manifested during readout. Generally, a two-electron system has four possible spin states when subjected to a magnetic field within a QD site. The four possible configurations are, namely, the singlet (S) and the three triplets (T_-, T_0, and T_+) states, as illustrated in Fig. 3(a). The difference in energy between the T_0 and the T_- (T_+) state is denoted as the Zeeman energy (ΔE_z), while E_{ST} denotes the energy difference between the S and T_0.

Fig. 3(b) depicts the corresponding orbital diagram for the two-electron system for the singlet and triplet states. Only the two lowest orbitals in which electrons can occupy are considered (i.e., O_1 and O_2). When the DQD is biased in the
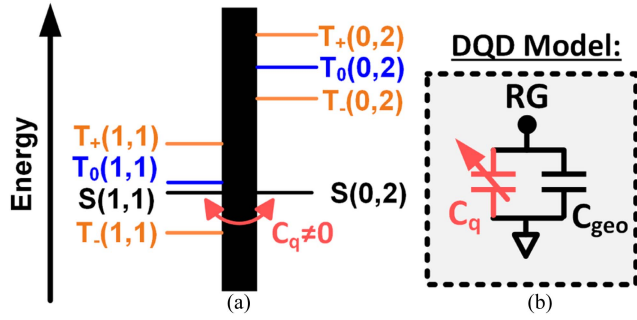
FIGURE 4. (a) Sketch of the singlet and triplet energy levels of the DQD for the (1,1) and (0,2) charge configurations. Due to the smaller E_{ST} of the (1,1) state compared with the (0,2) state, the lowest energy level of the DQD is $T_-(1,1)$ when $\epsilon = 0$ [12]. (b) Equivalent lump model of the DQD under RF excitation, comprising of a geometric capacitance (C_{geo}) and a state-dependent quantum capacitance (C_q).

(0,2) charge regime, these orbitals are spatially confined to only the right-hand side QD site, while they spread out across the DQD when biased in the (1,1) charge regime. Due to the Pauli exclusion principle, each orbital can only be occupied by two electrons of opposite spins [12]. Consequently, only the singlet state can contain two electrons occupying the same orbital.

The energy levels of the singlet and triplet configurations for the (1,1) and (0,2) charge configurations are plotted together in Fig. 4(a). The sketch's left- and right-hand side columns indicate the singlet and triplet energy levels for the (1,1) and (0,2) charge configurations, respectively. The figure illustrates when the DQD is at the interdot regime, equivalently described as the zero detuning condition ($\epsilon = 0$). Here, the detuning parameter (ϵ) is defined as the energy difference between the S(1,1) state and the S(0,2) state. In case the DQD collapses to a singlet state, an electron from one QD can freely tunnel to another at the zero detuning as the S(1,1) and the S(0,2) states have similar energy levels. In contrast, an electron cannot oscillate back and forth when the DQD is in a triplet state, as there are no overlapping triplet states when $\epsilon = 0$.

As the electron moves between the QD sites due to an RF readout signal applied at RG, quantum capacitance is generated [13]. Consequently, the DQD can be modeled as two parallel capacitors during readout, as illustrated in Fig. 4(b), where the capacitance contribution comes from, namely, the geometric capacitance (C_{geo}) and the state-dependent quantum capacitance (C_q). Thus, modeling the readout behavior of the system relies on quantifying the impact of quantum capacitance, which is the main focus of the subsequent section.

B. QUANTUM CAPACITANCE THEORY

As defined in [14], the quantum capacitance exhibited by the DQD is expressed as

$$C_q = -\beta^2 \frac{\partial^2 E_{|\psi\rangle}}{\partial \epsilon^2} \tag{4}$$

where $E_{|\psi\rangle}$ is the energy level of the singlet or triplet state of a DQD, and β is the lever arm of the DQD device, and is given by

$$\beta = |e| C_g / C_\Sigma \tag{5}$$

where $|e|$ is the electron charge, C_g is the capacitance of the RG, and C_Σ is the total geometric capacitance of the DQD.

To calculate the quantum capacitance contribution from the singlet or triplet state expressed in (4), the energy level of the DQD for different detunings must be calculated in each respective configuration. This can be achieved by solving the DQD's Hamiltonian using the Fermi–Hubbard model [15]. However, solving the total Fermi–Hubbard Hamiltonian of the DQD can be too complex and cumbersome. As we are only interested in the relevant features of the DQD under readout conditions, we simplify the DQD model and approximate the behavior by examining the Hamiltonian of a five-level system consisting of the ground and excited states of the S(1,1)–S(0,2) state and the three (1,1) triplet states. In general, the Hamiltonian for the S(1,1)–S(0,2) singlet state can be expressed by

$$H_{DQD,|S\rangle} = \frac{\epsilon}{2} \tau_z + t_c \tau_x \tag{6}$$

where t_c is the tunnel coupling, and $\tau_{z,x}$ are the Pauli matrices [16]. By solving the Hamiltonian with the time-independent Schrodinger equation, one can obtain the energy levels of the DQD for the singlet state as a function of detuning, expressed as

$$E_{|S_{g,e}\rangle} = \mp \frac{1}{2} \sqrt{\epsilon^2 + 4t_c^2}. \tag{7}$$

Furthermore, the energy levels of the (1,1) triplet state as a function of detuning can be approximated by [13]

$$E_{|T_0\rangle} = \frac{\epsilon}{2} \tag{8}$$

$$E_{|T_\pm\rangle} = \frac{\epsilon}{2} \pm g\mu_B B \tag{9}$$

where g is the electron gyromagnetic ratio, μ_B is the Bohr magneton constant, and B is the applied magnetic field.

The energy levels of the singlet and triplet states expressed in (7)–(9) as a function of the detunings are plotted in Fig. 5. By plugging the energy expression (7)–(9) to (4), the induced quantum capacitance of the singlet and triplet states can be, respectively, derived as

$$C_q = \begin{cases} +\beta^2 \dfrac{2t_c^2}{(\epsilon^2 + 4t_c^2)^{3/2}}, & \text{for } |S_g\rangle \quad (10) \\[3mm] -\beta^2 \dfrac{2t_c^2}{(\epsilon^2 + 4t_c^2)^{3/2}}, & \text{for } |S_e\rangle \quad (11) \\[3mm] 0, & \text{for } |T_0\rangle \text{ and } |T_\pm\rangle. \quad (12) \end{cases}$$

Note that only the singlet state contributes an additional quantum capacitance during readout due to the curvature of the energy level. Moreover, the ground singlet state produces a positive quantum capacitance, whereas the excited singlet
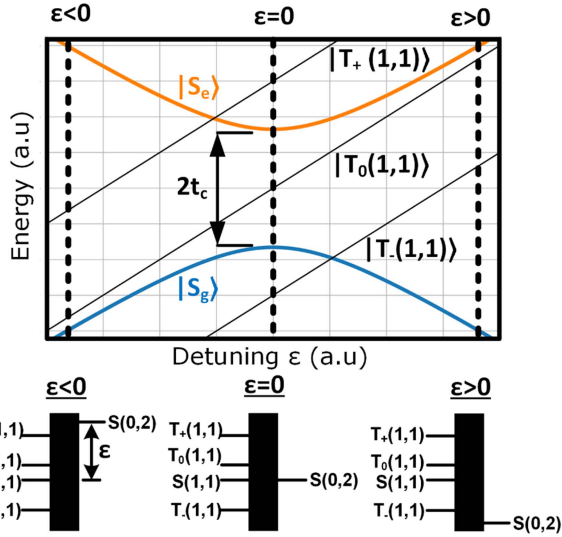
FIGURE 5. Energy level diagram of a DQD based on the two-level quantum system approximation. Note that the triplet (0,2) energy levels are not plotted as they are significantly higher than the (1,1) triplet energy levels.
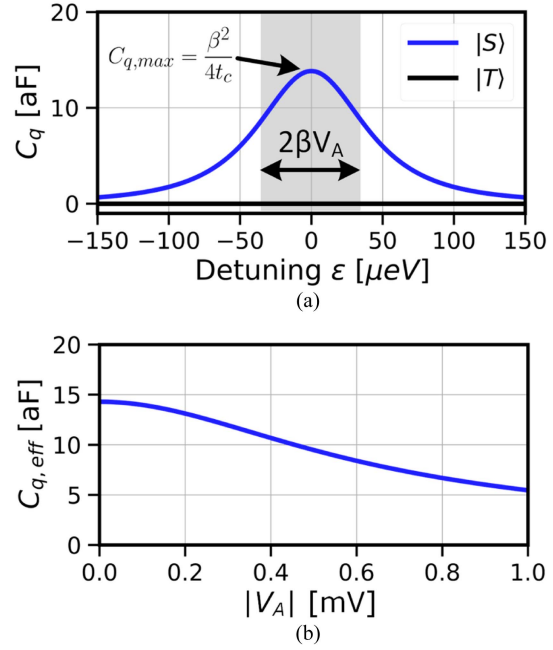

FIGURE 6. (a) Instantaneous quantum capacitance of the DQD with respect to the detuning of the DQD. (b) Effective quantum capacitance versus the signal amplitude ($|V_A|$) at the RG when the DQD is probed with a sinusoidal voltage with zero dc offset at zero-detuning bias.

state produces a negative quantum capacitance. In contrast, no quantum capacitance contribution exists when the DQD is in the triplet states, as their energy levels are linearly dependent on ϵ.

As previously mentioned, the right-hand side QD can be used as a reference spin for readout, in which its spin is initialized to a spin down and is used to compare the spin state of the left-hand side QD. Consequently, the two lowest energy levels used as the computational basis are the $|S_g\rangle$ and $|T_-\rangle$ states [see Fig. 3]. For convenience, the two computational basis states used for the analysis are referred to as the $|S\rangle$ and the $|T\rangle$ state for the rest of this article unless stated otherwise.

Based on the developed equations and theory for quantum capacitance, we can discuss and model the DQD behavior during readout in the following section.

C. QUANTUM CAPACITANCE DURING READOUT

In practice, the readout operation involves averaging the signal response of the system over many RF cycles to increase the SNR. Since the signal is averaged during readout acquisition, the quantum capacitance that the DQD contributes is also effectively averaged out. To illustrate this, based on (10), the quantum capacitance profile versus ϵ is illustrated in Fig. 6(a). Under the assumption that the RG is driven by a signal in the form of $V_A \sin(\omega_{RF}t)$, the detuning value changes sinusoidally over each RF cycle

$$\epsilon = \beta V_A \sin(\omega_{RF}t) \qquad (13)$$

in which, the role of the lever arm (β) is to convert voltage quantities to energy, with V_A denoting the signal's amplitude, and ω_{RF} as the angular frequency of the applied signal. Consequently, as shown in Fig. 6(a), the value of the quantum

capacitance varies along the shaded region due to the sinusoidal excitation. Due to the readout acquisition's averaging nature, the quantum capacitance's effective value seen during readout is the weighted average of the quantum capacitance value across the shaded region. By substituting (13) into (10), the effective quantum capacitance can be expressed as

$$C_{q,\text{eff}} = \frac{1}{T_{\text{int}}} \int_0^{T_{\text{int}}} C_{q,|S_g\rangle}(\epsilon) \, dt \bigg|_{\epsilon = \beta V_A \sin(\omega_{RF}t)}. \qquad (14)$$

Provided that the integration time is an integer multiple of the RF readout signal's period (i.e., $T_{\text{int}} = nT_{RF}$), a closed-form expression for $C_{q,\text{eff}}$ can be obtained

$$C_{q,\text{eff}} = \frac{\beta^2 t_c \times E\left(2\pi, \frac{-\beta^2 V_A^2}{4t_c^2}\right)}{2\pi(\beta^2 V_A^2 + 4t_c^2)} \qquad (15)$$

where $E(\theta, k)$ is an elliptical integral expressed as

$$E(\theta, k) = \int_0^\theta \sqrt{1 - k^2 \sin\theta} \, d\theta. \qquad (16)$$

The effective capacitance for different readout amplitudes is plotted in Fig. 6(b), which is based on the result of (15). A smaller readout excitation is observed to induce a larger effective quantum capacitance due to the smaller averaging window, which only captures the peak of the quantum capacitance profile. At small readout voltages, $C_{q,\text{eff}}$ converges to $\beta^2/4t_c$, in line with (10) when $\epsilon = 0$. Also, note that a small readout excitation degrades the readout signal [see (2)], which may reduce the SNR for a given fixed T_{int}. Hence,
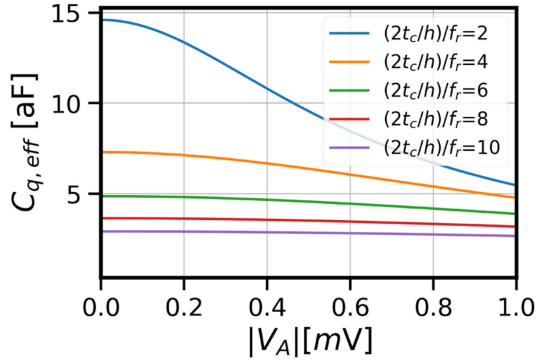
FIGURE 7. $C_{q,\text{eff}}$ for different adiabaticity factors [i.e., $(2tc/h)/f_r$] versus different signal amplitude ($|V_A|$), for a fixed readout frequency (f_r) of 6.91 GHz.

a longer T_{int} may be required to regain the same SNR. In contrast, a larger readout excitation implies a smaller effective quantum capacitance, which may, in effect, decrease the frequency shift of the response between the $|S\rangle$ and $|T\rangle$ states. This behavior is reflected in the state-separation factor between the $|S\rangle$ and $|T\rangle$ and consequently may lower the SNR, as described in (2).

D. OPTIMUM TUNNEL COUPLING

It should be noted that the tunnel coupling can significantly influence the behavior of the qubit during readout. When the tunnel coupling is set too low, the energy gap between the $|S_e\rangle$ band and the $|S_g\rangle$ band diminishes [see Fig. 5]. As the $|S_e\rangle$ band gets closer to the $|S_g\rangle$ state, the system can transition between the $|S_e\rangle$ and $|S_g\rangle$ energy bands instead of staying in the $|S_g\rangle$ band, which is necessary for the system to realize quantum capacitance. For the assumption presented here to be valid, the system must be biased in the adiabatic limit, bounded by $(2t_c/h)/f_r > 1$ [13], where f_r is the readout frequency and h is the Planck constant. The system is more adiabatic and less likely to transition between the $|S_e\rangle$ and $|S_g\rangle$ states as the ratio between the tunnel coupling and the readout frequency f_r increases.

The $C_{q,\text{eff}}$ for different adiabaticity factors, here expressed as $(2t_c/h)/f_r$, are plotted in Fig. 7. While it is beneficial to bias the system above the adiabatic limit to keep the system in the $|S_g\rangle$ energy band, a larger quantum capacitance is observed by biasing the DQD closer to the limit, which can increase the readout sensitivity. Based on the observation, the qubit must be biased close to the adiabatic limit (i.e., $(2t_c/h)/f_r = 2$) to maximize the quantum capacitance contribution.

E. LEVER ARM

The quantum capacitance can also be increased by means of the lever arm (β) to increase the readout sensitivity, as described by (10). The lever arm can be increased by designing the QD devices with quantum wells closer to the gate electrodes or by implementing the device in a silicon substrate, similar to a CMOS process [17], [18]. While the approach
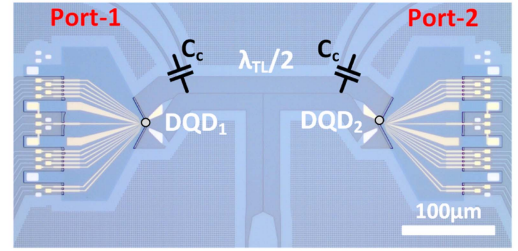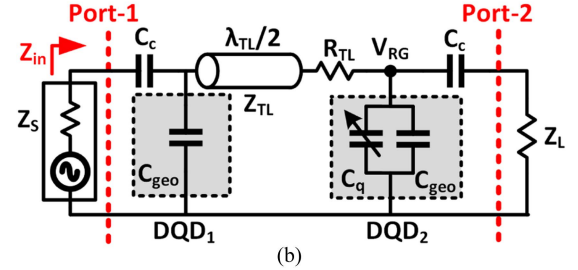
FIGURE 8. (a) Micrograph of the sample. The resonator consists of a narrow NbTiN $\lambda/2$ transmission line and has two capacitively coupled ports (i.e., Port-1 and Port-2). The endpoints of the resonator are connected to RG of DQD$_1$ and DQD$_2$ [see Fig. 2]. The gold-colored features are the fan-out of the plunger gates of the DQDs. (b) Equivalent circuit model of the sample when DQD$_1$ is detuned and DQD$_2$ biased in the interdot regime.

aligns well with the future goal of monolithic integration with CMOS electronics, these devices tend to have faster decoherence times as the qubit is located closer to the gate dielectric interface [18]. Thus, increasing the lever arm will need careful consideration as it influences multiple factors other than the readout performance.

III. READOUT SIMULATION

The quantum capacitance model introduced in the previous section can now be applied to a qubit sample that has been measured previously [19]. The qubit micrograph is shown in Fig. 8(a). The sample, realized in ^{28}Si/SiGe heterostructure, consists of two DQD sites separated by a 250 μm half-wavelength superconducting transmission line fabricated with NbTiN material. The half-wavelength transmission line is ac coupled to the input and output ports (port-1 and port-2) through the coupling capacitors C_c. The DQD$_2$ is biased at the zero detuning regime, thus exhibiting a geometric and quantum capacitance during readout when DQD$_2$ is at the $|S\rangle$ state. Moreover, the DQD$_1$ is tuned in the (0,0) charge regime, and thus only contains a fixed geometric capacitance. The sample is probed with an RF signal from port-1. The RF tone's corresponding phase or amplitude change can be detected by measuring its in-phase (I) and quadrature (Q) signal components at port-2 using an I/Q RX.

The complete electrical model of the sample is shown in Fig. 8(b). To model the state-dependent capacitance of DQD$_2$, a voltage-dependent capacitor $C_q(V_{\text{RG}})$ is included in the circuit, and its value depends on the voltage at the RG [see Fig. 2]. A resistor (i.e., R_{TL}) is also included in series to

TABLE 1. System Parameters for Simulation and Verification

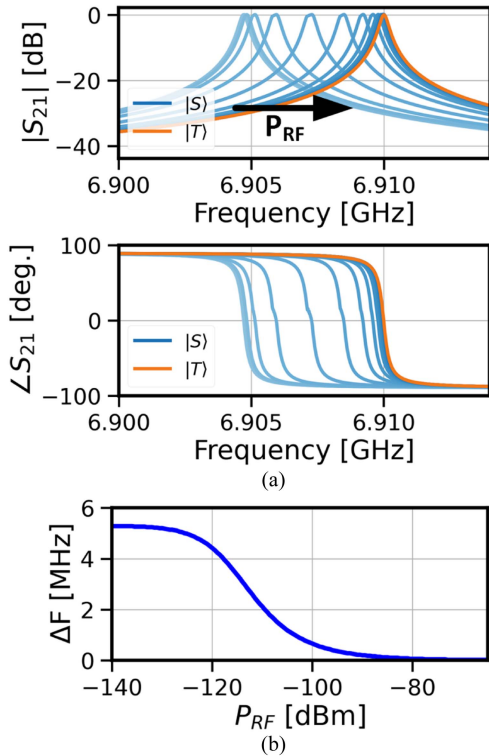| Quantity, Symbol	Value
Tunnel coupling, $2t_c/h$	14.1 GHz
Lever arm, β	102 meV/V
Characteristic resonator impedance, Z_{TL}	4.5 kΩ
Characteristic impedance of system, Z_0	50 Ω
Geometric DQD capacitance, C_{geo}	1.9 fF
Coupling capacitance, C_c	0.32 fF
Series resistance, R_{TL}	17 Ω

FIGURE 9. (a) Simulated magnitude and phase response of the transmission gain (S_{21}) versus frequency of the readout system in Fig. 8 for P_{RF} of -140 to -60 dBm in steps of 5 dBm. (b) Frequency shift between the $|S\rangle$- and $|T\rangle$-state resonant frequencies for different RF input power.

the transmission line in the schematic to model the system's loss, which can originate from resistive and dielectric losses in the sample [20]. When comparing the simulation with the measurement results, R_{TL} is used as a fitting parameter based on the measured resonator's bandwidth. In the simulation, the quantum capacitance contribution is realized by a lookup table VerilogA model, relating different RG voltage levels to distinct C_q values using (10) and DQD properties summarized in Table 1.

A. FREQUENCY SHIFT

The transmission (S_{21}) behavior between port-1 and port-2 for different P_{RF} values is plotted in Fig. 9(a). The orange and blue lines in the plot indicate the transmission response when the DQD is in the $|T\rangle$ and the $|S\rangle$ state, respectively.

To gain more insight into the (S_{21}) behavior, it is instructive to see the behavior of the input impedance of the sample.

For simplicity, a large coupling capacitor C_c and a lossless system are first considered such that the input impedance of the sample can be approximated as

$$Z_{\mathrm{in}} \approx Z_{\mathrm{TL,eff}} \frac{Z_L + jZ_{\mathrm{TL,eff}}\tan(\gamma l)}{Z_{\mathrm{TL,eff}} + jZ_L\tan(\gamma l)} \quad (17)$$

where l is the physical length of the transmission line, and Z_L is the load impedance (equal to 50 Ω). $Z_{\mathrm{TL,eff}}$ is the effective characteristic impedance of the transmission line defined as $\sqrt{L'_{\mathrm{TL}}/C'_{\mathrm{TL,eff}}}$, where L'_{TL} is the inductance per unit length, and $C'_{\mathrm{TL,eff}}$ is the effective capacitance per unit length of the transmission line, including the capacitance of the DQD. In addition, γ is the phase constant defined as

$$\gamma = \omega\sqrt{L'_{\mathrm{TL}}C'_{\mathrm{TL,eff}}} \quad (18)$$

where ω is the angular frequency where the expression is evaluated. On resonance, (17) simplifies to 50 Ω as $\tan(\gamma l)$ approaches 0. In effect, all the power provided by the source (P_{RF}) is delivered to port-1 and consequently also delivered to the load at port-2, resulting in a 0 dB response in the $|S_{21}|$ plot [see Fig. 9(a)]. Away from resonance, $\tan(\gamma l)$ tends to be large, thus Z_{in} approaches $\sim Z^2_{\mathrm{TL,eff}}/Z_L$. Due to the system's large $Z_{\mathrm{TL,eff}}$, reflection at the input plane occurs, leading to an incomplete power transfer to Z_L. This reflection contributes to the observed bandpass response in the $|S_{21}|$ plot.

The resonant condition requires that the γl term in (17) be equivalent to π, such that Z_{in} simplifies to 50 Ω. Consequently, the resonant frequency can be derived based on (18) and can be recast as

$$\omega_{\mathrm{res}} = \frac{\pi}{\sqrt{(L'_{\mathrm{TL}}l) \times (C'_{\mathrm{TL,eff}}l)}} \rightarrow \omega_{\mathrm{res}} = \frac{\pi}{\sqrt{L_{\mathrm{TL}}C_{\mathrm{TL,eff}}}} \quad (19)$$

where L_{TL} and $C_{\mathrm{TL,eff}}$ are the transmission line's total equivalent *lumped* inductance and capacitance, respectively. Note that $C_{\mathrm{TL,eff}}$ has two different loading conditions depending on the state of the DQD$_2$, which can be described as

$$C_{\mathrm{TL,eff}} = \begin{cases} C_{\mathrm{TL},|T\rangle} = C_{\mathrm{TL}} + 2C_{\mathrm{geo}}, & |T\rangle \text{ state} \\ C_{\mathrm{TL},|S\rangle} = C_{\mathrm{TL}} + 2C_{\mathrm{geo}} + C_q, & |S\rangle \text{ state} \end{cases} \quad (20)$$

where C_{TL} is the equivalent lumped capacitance of only the bare transmission line, excluding the DQD's contribution.

When DQD$_2$ is in the $|T\rangle$ state, $C_{\mathrm{TL,eff}}$ is only affected by C_{geo}. On the other hand, when DQD$_2$ is at the $|S\rangle$ state, $C_{\mathrm{TL,eff}}$ is affected by C_{geo} and C_q, which leads to a lower ω_{res}, as observed from Fig. 9(a). In addition, when the system is subjected to a strong RF readout signal, C_q is averaged over a larger span. This results in a lower $C_{q,\mathrm{eff}}$, causing a smaller resonant frequency separation between the $|S\rangle$ and the $|T\rangle$ response.

To further increase the separation of the resonant frequency between the $|T\rangle$ and $|S\rangle$ states, it is necessary to increase the $C_{\mathrm{TL},|S\rangle}/C_{\mathrm{TL},|T\rangle}$ capacitance ratio. Hence, C_q must be maximized while keeping C_{TL} and C_{geo} low. A higher C_q
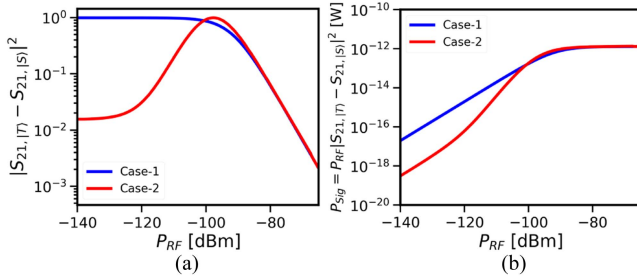
FIGURE 10. Simulated readout response. (a) State-separation factor versus readout power (P_{RF}). (b) Received power at port-2 of the transmission line (i.e., P_{Sig}) versus P_{RF}. Larger P_{RF} results in similar P_{sig} as the $|S\rangle$ and the $|T\rangle$ resonant frequency converges.

can be achieved by increasing the lever arm of the device with the drawbacks mentioned in Section II. On the other hand, C_{TL} can be kept low by designing the transmission line with a large characteristic impedance.

The simulated resonant frequency shift difference (i.e., ΔF) of the $|S\rangle$-state relative to the $|T\rangle$-state for different input probe power is summarized in Fig. 9(b). At low readout power, a $\sim$5 MHz frequency shift is seen. However, the frequency shift becomes smaller at higher probe power as $C_{TL,|S\rangle}$ approaches $C_{TL,|T\rangle}$, which aligns with the presented theory.

B. READOUT SIGNAL AND PROBE FREQUENCY

To determine the readout SNR, the readout signal's power at port-2 must be calculated. However, the behavior of the readout signal depends on the frequency at which the system is probed. This section explores the behavior of the readout signal in two scenarios: 1) when the system is probed at the resonant frequency of state $|T\rangle$ (i.e., 6.91 GHz) leading to a BASK response and 2) at the frequency halfway in between the resonant frequency response of the $|S\rangle$ and $|T\rangle$ states, leading to a BPSK response.

As expressed in (1), the readout signal's power (P_{sig}) is defined as the product of the state-separation factor and the power applied to the readout sample. The simulated state-separation factor (i.e., $|S_{21,|T\rangle}(\omega_r) - S_{21,|S\rangle}(\omega_r)|^2$) for both cases are plotted in Fig. 10(a). In case-1, the state-separation factor is shown to be approximately 1 for low readout probe power. In this condition, the $S_{21,|S\rangle}$ term is significantly smaller than the $S_{21,|T\rangle}$ term when probed at the resonance of the $|T\rangle$ state. Consequently, the $|S\rangle$ response is attenuated during readout compared with the $|T\rangle$ response, resembling a BASK readout signal, as discussed previously. In case-2, the state-separation factor is shown to be smaller than case-1 at low readout power. In this condition, both the $S_{21,|T\rangle}$ and $S_{21,|S\rangle}$ terms are generally small when probed between the $|T\rangle$ and $|S\rangle$ resonant frequencies. This results in a readout response that is both attenuated and exhibits a 180° phase difference between the $|T\rangle$ and $|S\rangle$ readout responses, similar to a BPSK signal. Interestingly, as the applied input power increases, the state-separation factor converges, reflecting that the resonant frequencies of the $|T\rangle$ and $|S\rangle$ states converge.

The readout signal's power is shown in Fig. 10(b). Remarkably, the plot shows a saturation in the readout signal power due to the decrease in the state-separation factor with the application of higher readout probe power. As the readout signal power dictates the readout SNR [see (2)], the simulation implies that there is a maximum achievable SNR for a given qubit property. Interestingly, in a different way and based on the time-dependent charge population in the DQD under RF excitation, Derakhshan et al. [21] also theoretically predicted the saturation in the readout signal. However, the work in [21] did not consider the power-dependent frequency shift and did not present any experimental results to support the theory.

From this observation, performing a readout shown by case-1 is generally recommended, as it yields a larger readout signal response even at lower probe power, leading to a higher SNR even at lower probe power. Furthermore, from a practical point of view, readout at the bare resonant peak of the resonator is simpler as the readout frequency is fixed and does not need to be changed to account for the power-dependent resonant shift. Based on this reasoning, the experiments in this article follow the readout behavior shown by case-1.

C. NOISE ESTIMATION

The power spectral density of the system's noise (N_0) at the input of the readout chain can be expressed as kT_N(W/Hz), where k is the Boltzmann constant, and T_N is the effective noise temperature of the readout system. Considering an ambient temperature of T_{amb} for the DQD sample, T_N may be estimated by

$$T_N = T_{amb} + T_{TWPA} + \frac{T_{LNA}}{G_1} + \frac{T_{RX}}{G_1 G_2} \qquad (21)$$

where T_{TWPA}, T_{LNA}, and T_{RX} are the noise temperatures of the traveling wave parametric amplifier (TWPA), low noise amplifier (LNA), and the RX, respectively, while G_1 and G_2 are the gain of the TPWA and LNA, respectively. Considering a TWPA gain of 28 dB (G_1), the readout system's noise performance is mainly dictated by the TWPA. Assuming that the TWPA is quantum-limited, its noise temperature can be approximated by $T_{TWPA} = hf_r/k$ [22]. For an f_r of 6.91 GHz, and a T_{amb} of 20 mK, the total noise temperature of the readout architecture (T_N) is estimated to be 350 mK.

D. NORMALIZED SNR

The behavior of the readout SNR can now be discussed. However, to properly evaluate the tradeoff between P_{RF} and N_0, it is far more instructive to define the normalized SNR: $SNR_N = P_{Sig}/N_0 = SNR/T_{int}$. In this way, we can compare the performance of the readout scheme independent of the chosen T_{int}. The simulated SNR_N, when assuming a T_N of 350 mK and considering all the system parameters in Table 1, is plotted in Fig. 11. The SNR_N first increases linearly with the probe power but finally saturates at a maximum of $\sim$95 dB·Hz. Considering a T_{int} of 1 μs, and assuming a
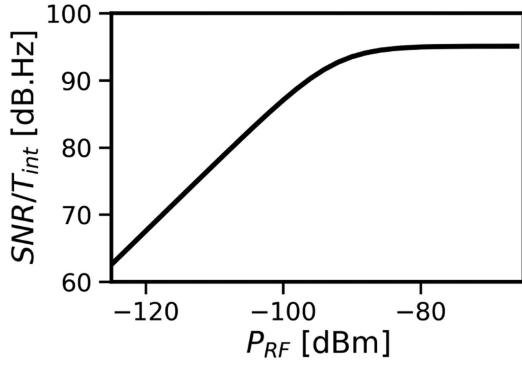
FIGURE 11. Simulated normalized SNR (SNR/T_{int}) versus input readout power (P_{RF}), assuming a quantum-limited readout chain and an effective noise temperature (T_N) of 350 mK.
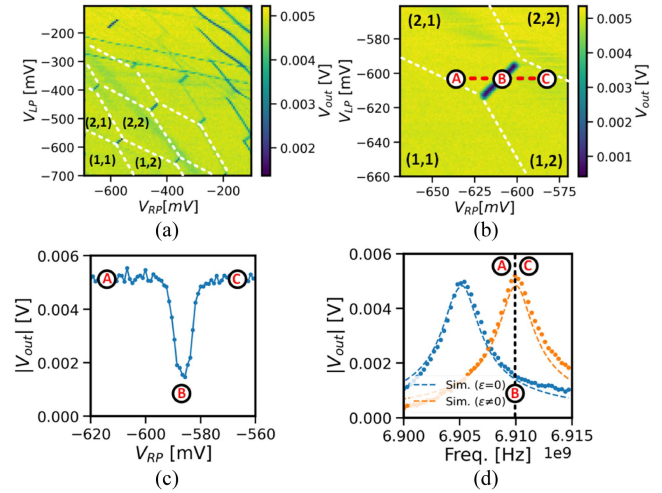

FIGURE 12. Measurement setup used to verify the quantum capacitance behavior.

FIGURE 13. (a) Measured charge stability diagram of DQD$_2$. $|V_{out}|$ obtained from I_{out} and Q_{out} voltages at the RT plane [see Fig. 12]. (b) Zoomed-in charge stability diagram at (2,1)–(1,2) charge regime, where the dark blue line indicates the regime in which an electron can move freely back and forth between the two dots in response to an applied excitation, changing the quantum capacitance and hence measured signal. The next two subfigures are measured across the red dashed line: (c) $|V_{out}|$ versus V_{RP} and (d) $|V_{out}|$ versus frequency at zero and nonzero detuning.
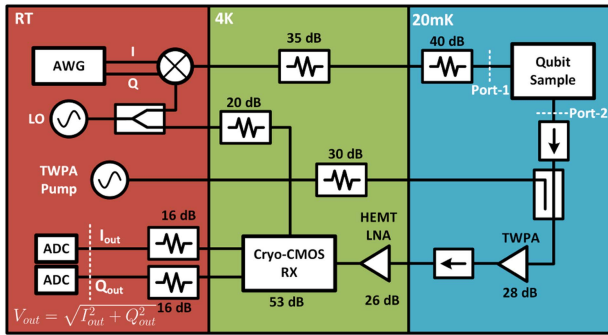
quantum-limited readout chain, a theoretical maximum SNR of 35 dB is achievable.

With the theoretical framework for gate-based RF readout established, the measurement verification of the proposed model can now be carried out.

IV. MEASUREMENTS

A. MEASUREMENT SETUP

The complete measurement setup is shown in Fig. 12, similar to the ones used in [19], [20], and [23]. The sample is mounted at the mixing chamber plate and cooled down to an ambient temperature of 20 mK. Alongside the qubit sample, a TWPA with 28 dB gain is installed to minimize the noise of the readout chain, thus allowing one to measure a low-power readout signal at various T_{int}. The TWPA pump is generated at room temperature (RT) and fed to the TWPA by a coupler at the mixing chamber plate. An isolator is used between the qubit sample and the coupler to isolate the qubit from reflections due to the large TWPA pump tone. At the 4 K plate, a high electron mobility transistor (HEMT) LNA with a 26 dB of gain is used to amplify the readout signal further. An additional CMOS RX chip is mounted on this plate for signal downconversion and amplification [23]. At RT, two off-the-shelf 1 GS/s 8-b analog to digital converters (ADCs) are used to quantize both the I/Q signals, allowing for further

digital signal processing at the baseband. A single local oscillator (LO) source at RT is also used to drive the two mixers that upconvert and downconvert the readout signal to ensure phase synchronization. Moreover, a 75-dB attenuation in the input RF line is intentionally employed to ensure a proper thermal noise level at the input of the sample at the mixing chamber plate.

B. CHARGE STABILITY DIAGRAM

In this work, the proposed model is evaluated by emulating the $|S\rangle$ and $|T\rangle$ states discussed previously based on whether the resonator is loaded or unloaded with quantum capacitance. Such an approach ensures that the verification of our proposed model is decoupled from additional errors, such as initialization and relaxation errors. Consequently, we do not emulate the $|S\rangle$ and $|T\rangle$ states by randomly loading the DQD with electrons and executing a single-shot readout [9]. Instead, the model is verified by observing the response of the DQD when it is biased in or out of the interdot regime. To find the interdot regime of the DQD, the charge stability diagram of the sample needs to be first measured.

The stability diagram of the sample is measured and shown in Fig. 13(a). The diagram is obtained when the sample is read out at the bare resonance frequency (i.e., 6.91 GHz) for different V_{LP} and V_{RP} values. A clear distinction between different charge states can be observed, especially at lower charge population regimes.

The behavior of $C_{q,eff}$ is verified in the (2,1)–(1,2) charge state. Considering that the quantum capacitance is generated by forcing an electron to oscillate across the DQD site under RF excitation, the behavior in the (2,1)–(1,2) regime is

similar to the (1,1)–(0,2) regime discussed previously since the experiment isolates only the quantum capacitance contribution behavior. The charge stability scan around the (2,1)–(1,2) charge state is shown in Fig. 13(b). To understand the effect of the quantum capacitance during readout, a line cut is taken across the interdot crossing, and its corresponding result is depicted in Fig. 13(c). At point (A), the DQD is not loaded by the quantum capacitance as it is far from the zero detuning ($V_{\text{RP}} = -620$ mV). As shown previously, averaging the quantum capacitance well away from the zero detuning results in a net zero effective quantum capacitance, which emulates the behavior of the $|T\rangle$ state. In contrast, point (B) is located where the system is at zero detuning ($V_{\text{RP}} = -590$ mV), where the maximum quantum capacitance contribution can be observed. In this region, the sample emulates the behavior of the $|S\rangle$ state. Due to the quantum capacitance contribution, the resonator's resonance frequency shifts to a lower frequency, which, in effect, lowers the observed output voltage. As more positive V_{RP} is applied to the DQD ($V_{\text{RP}} = -560$ mV), the system returns to the response observed at (A).

The shift in the resonance frequency of the resonator can also be observed in Fig. 13(d). The data are obtained by monitoring the magnitude of the downconverted I/Q voltages (i.e., $|V_{\text{out}}|$) when the frequency of the probe signal is swept from 6.9 to 6.915 GHz. For comparison, the simulation results are also included in Fig. 13(d) using the dotted lines, which show a good agreement with the measurements. The orange line in the figure depicts the response when the system is away from zero detuning ($V_{\text{RP}} = -620$ mV), while the blue line depicts the system's response at zero detuning ($V_{\text{RP}} = -590$ mV). The mapping of points (A)–(C) from Fig. 13(c) are also labeled in Fig. 13(d) for clarity. As predicted from the simulation, a 5-MHz frequency shift is observed for the zero-detuning response at very low power.

C. FREQUENCY SHIFT

Given that the quantum capacitance cannot be measured directly, we can only observe the manifestation of the quantum capacitance through the frequency shift response of the sample. To verify this, the frequency at which the maximum transmission is observed is tracked at zero detuning and nonzero detuning conditions while sweeping the probe tone power from -125 to -89 dBm, referred to the port-1 plane in Fig. 12(c). The frequency difference (ΔF) is defined as the difference between the resonance peaks of the nonzero and zero detuning responses. As shown in Fig. 14, the frequency shift of the DQD decreases for higher input power, following the trajectory dictated by the developed theory and simulation results. Interestingly, the frequency shift reaches 0 faster than in the simulation. This behavior is discussed in the following section.

D. READOUT SIGNAL

The simulated and measured readout I/Q responses for zero and nonzero detunings are illustrated in Fig. 15(a). The data
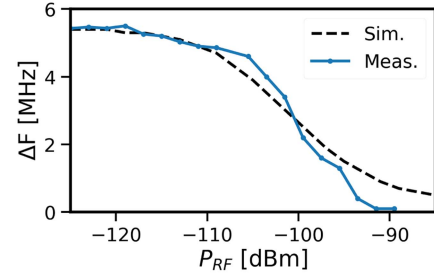

FIGURE 14. Observed frequency shift (ΔF) in simulation and measurements for different input readout power (P_{RF}). Larger readout power is seen to induce smaller ΔF due to lower quantum capacitance.
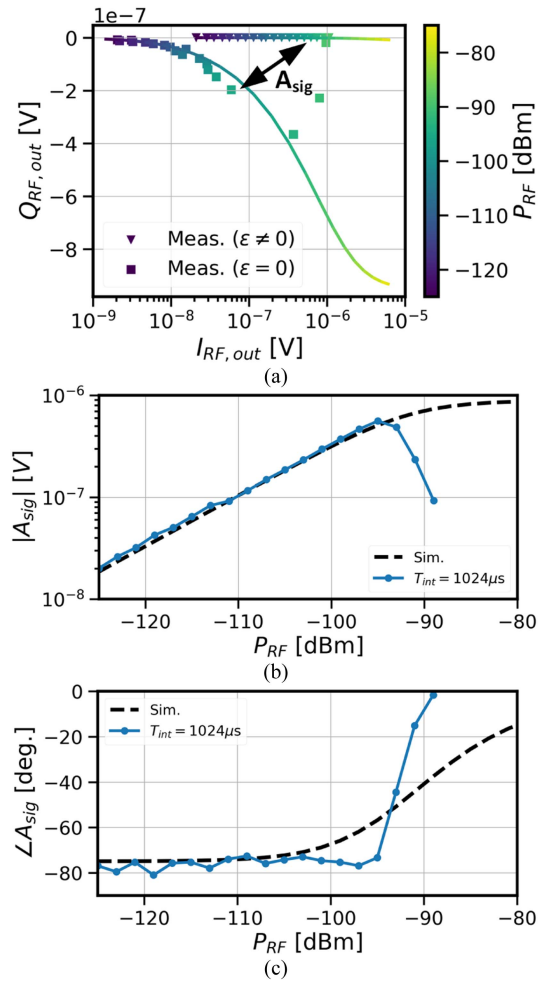

FIGURE 15. (a) I/Q trajectory of readout signal for different P_{RF} at zero and nonzero detuning regimes. The colored graded line indicates the expected I/Q trajectory from the simulation, while the triangle and the square data points indicate the measured value at nonzero and zero detuning, respectively. (b) Magnitude and (c) phase response of A_{sig}.

are obtained by referring the measured I/Q datasets to the port-2 plane when the system is probed at the readout frequency of $\omega_r/2\pi = 6.91$ GHz. The triangle and square points indicate the nonzero and zero-detuning responses, respectively. Note that the solid line indicates the simulated I/Q voltages, and the measured data points are color graded based on the readout power applied to the sample.

Based on Fig. 15(a), the I/Q points resemble an amplitude-modulated signal at lower readout power, where the zero-detuning response is close to the origin of the I/Q plane due to the attenuation of the shifted resonator response. At higher readout power, the zero-detuning I/Q response acquires an extra phase component as the resonant frequency of the zero-detuning response gets closer to the bare-resonance frequency of 6.91 GHz. The distance between the two responses is also reduced for the higher power, implying a decreased readout signal amplitude at a larger probe power.

As explained in Section I and shown in Fig. 15(a), the readout signal (A_{sig}) is the distance between the qubit's responses in the constellation diagram. The magnitude and phase of A_{sig} are, respectively, shown in Fig. 15(b) and (c). The simulated and measured $|A_{\text{sig}}|$ and $\angle A_{\text{sig}}$ are seen to be in good agreement up to P_{RF} of ∼-100 dBm. Beyond this point, a noticeable difference between simulation and measurement is observed, especially the measured $\angle A_{\text{sig}}$. Compared with the simulation, at large probe power, the measured $\angle A_{\text{sig}}$ approaches 0 degrees faster, and the measured $|A_{\text{sig}}|$ does not saturate but reduces significantly. Both magnitude and phase behaviors imply that the resonant frequency of the zero detuning response becomes the same as the bare resonance frequency of the resonator, consistent with the qualitative trend observed for ΔF in Fig. 14. The discrepancy between the measurement and the model is suspected to be due to self-heating effects [24] and Landau–Zener transitions [25], which are further discussed in Section V-A.

E. READOUT NOISE

The standard deviation of $|V_{\text{out}}|$ can be used to estimate T_N experimentally. By measuring the standard deviation of $|V_{\text{out}}|$ at the nonzero detuning regime between a V_{RP} of -570 to -560 mV [i.e., Point C in Fig. 13(c)], the integrated noise voltage can be calculated. Mathematically, this is equivalent to $\sqrt{kT_N \cdot 50/T_{\text{int}}}$ (V). Experimentally, T_N is estimated to be 460 mK when referring to the input of the readout chain.

The measured T_N is close to what was previously observed for a readout chain incorporating TWPA amplifiers [26], [27], [28]. However, it is $1.3\times$ higher than the previous theoretical estimation (i.e., 350 mK). The discrepancy between the theoretical and measured values may stem from different contributions. First, T_N is estimated by always assuming that T_{amb} is 20 mK, which may be higher in reality as reflected by the electron temperature. Moreover, the estimation did not account for the losses of the isolator and coupler in front of the TWPA.

F. NORMALIZED SNR

Fig. 16 shows the measured and simulated SNR_N. The black dotted line indicates the simulated SNR_N based on the previously simulated readout signal, with a T_N of 460 mK. As expected, the data show that the measured SNR_N overlaps each other for different T_{int} experiments. A maximum measured SNR_N of ∼89 dB · Hz is observed at $P_{\text{RF}} = -95$ dBm, and SNR_N degrades beyond this power level.
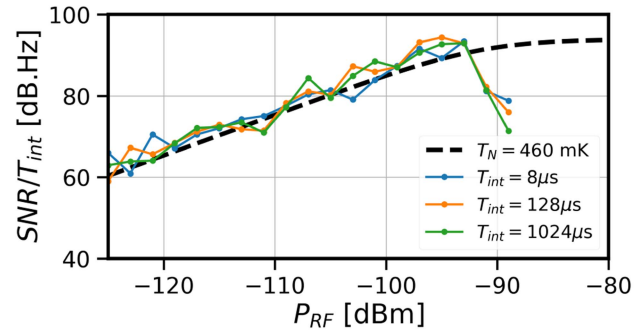

FIGURE 16. Measured normalized readout SNR ($\text{SNR}/T_{\text{int}}$) versus different input probe power (P_{RF}) and integration time (T_{int}). The black dotted line indicates the simulated normalized readout SNR, assuming an effective noise temperature (T_N) of 460 mK.

V. DISCUSSION

The previous section showed that the qubits' resonant frequency shift is power dependent. This section discusses the discrepancy observed between the measurement results and the proposed model, explores the implications of the power-dependent readout behavior, examines the associated trade-offs, and addresses the noise requirements for the readout chain.

A. REDUCED READOUT SIGNAL AT LARGE PROBE POWER

Measurements in Section IV-D indicate a drop in the readout signal for larger probe excitation, which the developed model in this work could not capture. This section discusses the possible reasons behind the drop of readout signal at large probe powers in terms of self-heating [24] and the Landau–Zener effect [25].

The self-heating effect can reduce A_{sig} by decreasing the quality factor of the bare-resonator at large readout excitation. Thus, to observe self-heating's contribution, the quality factor of the bare-resonator is monitored for different P_{RF} and adiabaticity factors, as shown in Fig. 17(a). Although, by increasing the probe power from -95 to -88 dBm, a ∼$1.6\times$ reduction in the resonator's quality factor is observed due to the resonator's elevated temperature, this behavior does not fully explain the ∼$8\times$ reduction of A_{sig} observed in Section IV-D.

To further investigate the sudden drop in the readout signal, A_{sig} is measured versus P_{RF} at various adiabaticity factors, as shown in Fig. 17(b). The measurement indicates that the drop in the readout signal occurs at lower P_{RF} for a smaller adiabaticity factor. It should be noted that if the reduction in the readout signal was purely due to self-heating, the drop in the readout signal would occur at the same P_{RF}, regardless of the adiabaticity condition. However, this is not the case here. Instead, the drop of the readout signal is influenced by the adiabaticity factor, a trend that is expected from Landau–Zener transitions.

Based on the Landau–Zener phenomenon, at a very large probe excitation, the rate at which the system's detuning evolves with time (i.e., $\partial \epsilon / \partial t$) becomes fast enough such
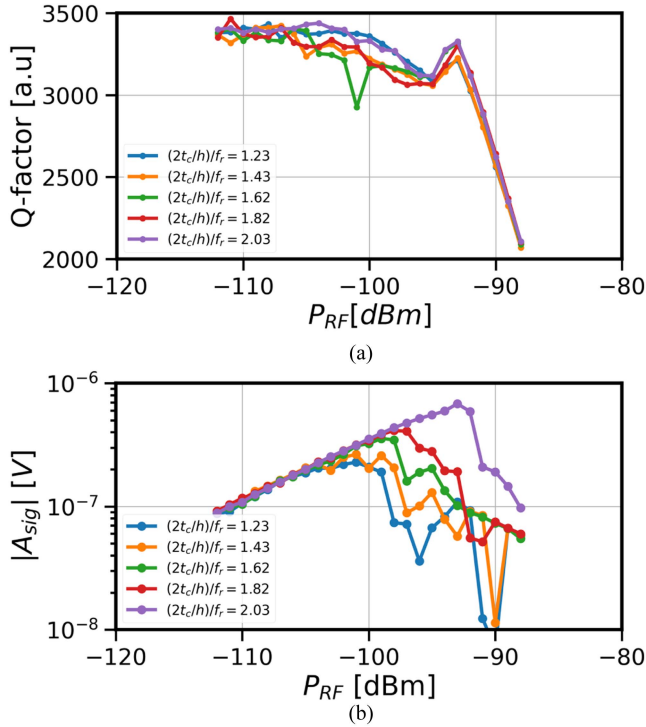
FIGURE 17. (a) Resonator's quality factor (Q-factor) at nonzero detuning and (b) readout signal ($|A_{sig}|$) versus the probe power (P_{RF}) for different adiabaticity factors. Note that the readout frequency (f_r) is 6.91 GHz for all measurements.

that the system's evolution becomes gradually nonadiabatic. Consequently, there will be a finite probability in which the system can undergo transitions between the $|S_g\rangle$ and $|S_e\rangle$ energy bands, similar to following the $|T_0\rangle$ trajectory, as illustrated in Fig. 5. This behavior can effectively reduce the quantum capacitance contribution toward 0, thereby reducing the readout signal.

The aforementioned description of the Landau–Zener phenomenon matches well with the trend, as shown in Fig. 17(b). A lower adiabaticity factor increases the likelihood of the system transitioning between the $|S_g\rangle$ and $|S_e\rangle$ states at large readout excitation [see Fig. 5]. Hence, the readout signal is seen to drop at lower P_{RF} when the adiabaticity factor is smaller. This observation is consistent with the theoretical work shown in [21], which also predicts that the quantum capacitance contribution can be reduced to 0 at large readout excitation when the system is tuned in the nonadiabatic regime, leading to a drop in the readout signal.

B. FREQUENCY MULTIPLEXING CONSIDERATION

The measurement and model indicate that the readout power can control the qubit's frequency shift. Thus, a higher readout power leads to the possibility of reading out more qubits per given bandwidth, resulting in a higher spectrum efficiency as the frequency spacing requirement between each qubit decreases. As depicted in Fig. 14, the frequency shift is estimated to be on the order of 2 MHz at the peak of the SNR_N with a P_{RF} of −95 dBm. Assuming each qubit has a

frequency shift of 2 MHz with a 3-MHz resonator bandwidth, each qubit has a channel bandwidth of ∼5 MHz. However, it should be noted the frequency spacing between the qubits cannot be too small as the readout pulse power, depending on the desired integration times, may leak into neighboring qubits, which eventually may require pulse shaping for a dense FDMA readout architecture.

It is important to note that the number of qubits that can be read out within a specific frequency range can be increased by narrowing the resonator bandwidth through a resonator design with a large characteristic impedance. However, there are practical constraints on how much the resonator bandwidth can be reduced. At a very small resonator bandwidth, readout is mostly limited by the ring-up time of the resonator when given an RF impulse. Consequently, the readout response may not settle fully for a given T_{int}, thus reducing the readout signal and, eventually, the SNR.

C. READOUT OPERATING FREQUENCY

Based on the discussion above, one could also ask about the preferable readout frequency for gate-based readout. Given a system with a readout frequency f_r and is biased at an adiabaticity factor of 2, a lower frequency shift is expected when the qubit is read out at higher f_r due to the lower quantum capacitance at higher t_c bias. In addition, a higher readout frequency increases the power consumption of the electronics significantly, which can also limit the scalability of the readout system due to the limited power budget in the dilution refrigerator. However, operating at a higher readout frequency may decrease the footprint of the resonator, which can be beneficial when the system is scaled up.

The opposite behavior is expected when the readout frequency is lowered while still keeping the same adiabaticity factor. A lower readout frequency implies a lower t_c. Hence, a larger quantum capacitance is to be expected, which can increase the SNR. As the frequency of operation is lowered, power consumption of the electronics is also expected to follow suit. However, the larger quantum capacitance means that each qubit occupies a larger channel and limits the number of qubits occupying a certain bandwidth. In addition, pushing the readout frequency lower leads to a larger area required for the resonator and may limit scalability.

D. NOISE TEMPERATURE REQUIREMENT FOR READOUT ELECTRONICS

As discussed in Section I, an SNR larger than 11.5 dB is needed to achieve BER $\leq 10^{-4}$. Assuming a T_{int} of 1 μs, the maximum inherent SNR of the measured gate-based readout is 29 dB, extrapolated from SNR_N of 89 dB · Hz [see Fig. 16]. Hence, an excess SNR of 17.5 dB allows one to increase N_0 by 56× and still satisfy the BER specification, resulting in a maximum T_N of 25.8 K for the readout chain. Furthermore, assuming that the readout electronics are now operating at 4 K, the readout chain should exhibit an input-referred noise temperature (T_{sys}) of $\leq$ 21.8 K to still comply with a readout
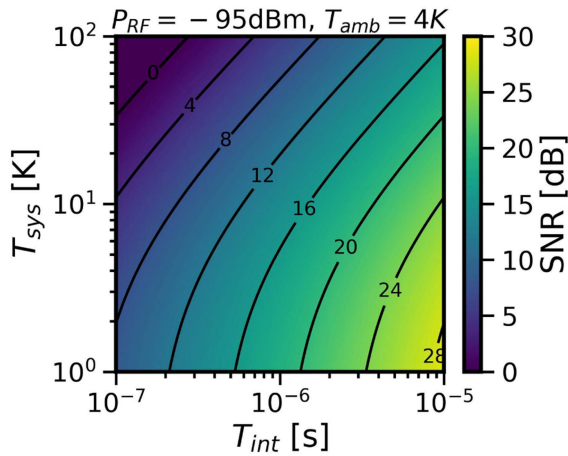
FIGURE 18. SNR contour plot for different integration time (T_{int}) and readout chain's noise temperature (T_{sys}) for an ambient temperature (T_{amb}) of 4 K and readout probe power (P_{RF}) of −95 dBm.

SNR of 11.5 dB—a significantly more relaxed noise requirement in comparison with the performance offered by TWPA and the HEMT LNA.

Fig. 18 shows the SNR for different T_{sys} and T_{int} values when the system is probed at its maximum achievable A_{sig} ($P_{RF} = -95$ dBm) while considering a T_{amb} of 4 K. Assuming a modest T_{sys} of 50 K based on the recently published cryo-CMOS RX design [23], [29], [30], [31], [32], the contour plot reveals that the prior-art cryo-CMOS RX cannot satisfy the 11.5 dB target SNR at a T_{int} of 1 μs. As it is suspected that the noise performance of the cryo-CMOS RX is limited by the shot noise [33] and the self-heating effect [34], passive amplification techniques should be investigated in the future to avoid large biasing currents required for active devices in LNAs [35], [36].

VI. CONCLUSION

This work presents a theoretical framework that allows one to investigate the impact of the RX's noise temperature, readout probe power, and integration time on the SNR and fidelity of RF gate-based readout systems. Considering the qubit's quantum mechanical behavior, a semiclassical model was developed that estimates the state- and power-dependent resonance frequency shifts and intrinsic readout SNR. Following the trajectory dictated by the developed theory and simulation, the experimental results showed that the frequency spacing between the resonance peaks corresponding to different qubit states was reduced by increasing the power of the readout tone. This affects the separation between the qubit states in the constellation diagram and eventually limits the maximum achievable SNR of the gate-based readout systems. Moreover, based on the outcome of this study, different tradeoffs among the qubit biasing, the readout SNR, the system's footprint, the RX's operating frequency, bandwidth, and noise are discussed. Consequently, the presented

guideline can help designers realize a scalable and low-power readout chain while obtaining a readout fidelity sufficient for fault-tolerant quantum computation.

REFERENCES

[1] A. G. Fowler, M. Mariantoni, J. M. Martinis, and A. N. Cleland, "Surface codes: Towards practical large-scale quantum computation," *Phys. Rev. A*, vol. 86, no. 3, 2012, Art. no. 0032324, doi: 10.1103/PhysRevA.86.032324.

[2] R. W. J. Overwater, M. Babaie, and F. Sebastiano, "Neural-network decoders for quantum error correction using surface codes: A space exploration of the hardware cost-performance tradeoffs," *IEEE Trans. Quantum Eng.*, vol. 3, May 2022, Art. no. 3101719, doi: 10.1109/TQE.2022.3174017.

[3] T. Struck et al., "Low-frequency spin qubit energy splitting noise in highly purified 28Si/SiGe," *Npj Quantum Inf.*, vol. 6, no. 1, pp. 1–7, doi: 10.1038/s41534-020-0276-2.

[4] J. Yoneda et al., "A quantum-dot spin qubit with coherence limited by charge noise and fidelity higher than 99.9%," *Nature Nanotechnol.*, vol. 13, no. 2, pp. 102–106, doi: 10.1038/s41565-017-0014-x.

[5] X. Xue et al., "Quantum logic with spin qubits crossing the surface code threshold," *Nature*, vol. 601, no. 7893, pp. 343–347, doi: 10.1038/s41586-021-04273-w.

[6] R. Li et al., "A crossbar network for silicon quantum dot qubits," *Sci. Adv.*, vol. 4, no. 7, 2018, Art. no. eaar3960, doi: 10.1126/sciadv.aar3960.

[7] A. Ruffino, T.-Y. Yang, J. Michniewicz, Y. Peng, E. Charbon, and M. F. Gonzalez-Zalba, "A cryo-CMOS chip that integrates silicon quantum dots and multiplexed dispersive readout electronics," *Nature Electron.*, vol. 5, no. 1, pp. 53–59, doi: 10.1038/s41928-021-00687-6.

[8] J. M. Hornibrook et al., "Frequency multiplexing for readout of spin qubits," *Appl. Phys. Lett.*, vol. 104, no. 10, 2014, Art. no. 103108, doi: 10.1063/1.4868107.

[9] G. Zheng et al., "Rapid gate-based spin read-out in silicon using an on-chip resonator," *Nature Nanotechnol.*, vol. 14, no. 8, pp. 742–746, doi: 10.1038/s41565-019-0488-9.

[10] I. Ahmed et al., "Radio-frequency capacitive gate-based sensing," *Phys. Rev. Appl.*, vol. 10, Jul. 2018, Art. no. 0014018, doi: 10.1103/PhysRevApplied.10.014018.

[11] D. J. Ibberson et al., "Large dispersive interaction between a CMOS double quantum dot and microwave photons," *PRX Quantum*, vol. 2, May 2021, Art. no. 0020315, doi: 10.1103/PRXQuantum.2.020315.

[12] R. Hanson, L. P. Kouwenhoven, J. R. Petta, S. Tarucha, and L. M. K. Vandersypen, "Spins in few-electron quantum dots," *Rev. Modern Phys.*, vol. 79, no. 4, 2007, Art. no. 1217, doi: 10.1103/RevModPhys.79.1217.

[13] R. Mizuta, R. M. Otxoa, A. C. Betz, and M. F. Gonzalez-Zalba, "Quantum and tunneling capacitance in charge and spin qubits," *Phys. Rev. B*, vol. 95, no. 4, 2017, Art. no. 045414, doi: 10.1103/PhysRevB.95.045414.

[14] K. D. Petersson, C. G. Smith, D. Anderson, P. Atkinson, G. A. Jones, and D. A. Ritchie, "Charge and spin state readout of a double quantum dot coupled to a resonator," *Nano Lett.*, vol. 10, no. 8, pp. 2789–2793, 2010, doi: 10.1021/nl100663w.

[15] T. Hensgens et al., "Quantum simulation of a Fermi–Hubbard model using a semiconductor quantum dot array," *Nature*, vol. 548, no. 7665, pp. 70–73, doi: 10.48550/arXiv.1702.07511.

[16] M. A. Nielsen and I. L. Chuang, *Quantum Computation and Quantum Information*, 10th Ed., Cambridge, U.K.: Cambridge Univ. Press, 2010, doi: 10.1017/CBO9780511976667.

[17] F. Ansaloni et al., "Single-electron operations in a foundry-fabricated array of quantum dots," *Nature Commun.*, vol. 11, 2020, Art. no. 6399, doi: 10.1038/s41467-020-20280-3.

[18] T. Tanttu, and et al., "Controlling spin-orbit interactions in silicon quantum dots using magnetic field direction," *Phys. Rev. X*, vol. 9, 2019, Art. no. 021028, doi: 10.1103/PhysRevX.9.021028.

[19] P. Harvey-Collard, J. Dijkema, G. Zheng, A. Sammak, G. Scappucci, and L. M. Vandersypen, "Coherent spin-spin coupling mediated by virtual microwave photons," *Phys. Rev. X*, vol. 12, 2022, Art. no. 021026, doi: 10.1103/PhysRevX.12.021026.

[20] P. Harvey-Collard et al., "On-chip microwave filters for high-impedance resonators with gate-defined quantum dots," *Phys. Rev. Appl.*, vol. 14, Sep. 2020, Art. no. 0034025, doi: 10.1103/PhysRevApplied.14.034025.

[21] V. Derakhshan Maman, M. Gonzalez-Zalba, and A. Pályi, "Charge noise and overdrive errors in dispersive readout of charge, spin, and majorana qubits," *Phys. Rev. Appl.*, vol. 14, no. 6, 2020, Art. no. 064024, doi: 10.1103/PhysRevApplied.14.064024.

[22] A. R. Kerr, M. J. Feldman, and S.-K. Pan, "Receiver noise temperature, the quantum noise limit, and the role of the zero-point fluctuations," in *Proc. 8th Int. Symp. Space Terahertz Technol.*, 1997, pp. 101–111.

[23] B. Prabowo et al., "13.3 A 6-to-8GHz 0.17mW/qubit cryo-CMOS receiver for multiple spin qubit readout in 40 nm CMOS technology," in *Proc. IEEE Int. Solid- State Circuits Conf.*, vol. 64, pp. 212–214, doi: 10.1109/ISSCC42613.2021.9365848.

[24] B. Undseth et al., "Hotter is easier: Unexpected temperature dependence of spin qubit frequencies," *Phys. Rev. X*, vol. 13, Oct. 2023, Art. no. 041015, doi: 10.1103/PhysRevX.13.041015.

[25] C. Zener, "Non-adiabatic crossing of energy levels," *Proc. Roy. Soc. London. Ser. A., Containing Papers A Math. Phys. Character*, vol. 137, no. 833, pp. 696–702, 1932, doi: 10.1098/rspa.1932.0165.

[26] C. Macklin et al., "A near–quantum-limited Josephson traveling-wave parametric amplifier," *Science*, vol. 350, no. 6258, pp. 307–310, 2015, doi: 10.1126/science.aaa8525.

[27] S. Simbierowicz et al., "Characterizing cryogenic amplifiers with a matched temperature-variable noise source," *Rev. Sci. Instruments*, vol. 92, no. 3, 2021, Art. no. 034708, doi: 10.1063/5.0028951.

[28] T. C. White et al., "Traveling wave parametric amplifier with Josephson junctions using minimal resonator phase matching," *Appl. Phys. Lett.*, vol. 106, no. 24, 2015, Art. no. 242601, doi: 10.1063/1.4922348.

[29] A. Ruffino, Y. Peng, T.-Y. Yang, J. Michniewicz, M. F. Gonzalez-Zalba, and E. Charbon, "13.2 a fully-integrated 40-nm 5-6.5 GHz cryo-CMOS system-on-chip with I/Q receiver and frequency synthesizer for scalable multiplexed readout of quantum dots," in *Proc. IEEE Int. Solid-State Circuits Conf.*, 2021, pp. 210–212, doi: 10.1109/ISSCC42613.2021.9365758.

[30] J. Park et al., "A fully integrated cryo-CMOS SoC for state manipulation, readout, and high-speed gate pulsing of spin qubits," *IEEE J. Solid-State Circuits*, vol. 56, no. 11, pp. 3289–3306, Nov. 2021, doi: 10.1109/JSSC.2021.3115988.

[31] S. Van Winckel et al., "A 28 nm 6.5-8.1GHz 1.16mW/qubit cryo-CMOS system-an-chip for superconducting qubit readout," in *Proc. ESSCIRC- IEEE 48th Eur. Solid State Circuits Conf.*, 2022, pp. 61–64, doi: 10.1109/ESSCIRC55480.2022.9911493.

[32] K. Kang et al., "A 40-nm cryo-CMOS quantum controller IC for superconducting qubit," *IEEE J. Solid-State Circuits*, vol. 57, no. 11, pp. 3274–3287, Nov. 2022, doi: 10.1109/JSSC.2022.3198663.

[33] J. Gong, Y. Chen, E. Charbon, F. Sebastiano, and M. Babaie, "A cryo-CMOS oscillator with an automatic common-mode resonance calibration for quantum computing applications," *IEEE Trans. Circuits Syst. I: Reg. Papers*, vol. 69, no. 12, pp. 4810–4822, Dec. 2022, doi: 10.1109/TCSI.2022.3199997.

[34] P. A. T. Hart, M. Babaie, A. Vladimirescu, and F. Sebastiano, "Characterization and modeling of self-heating in nanometer bulk-CMOS at cryogenic temperatures," *IEEE J. Electron Devices Soc.*, vol. 9, pp. 891–901, Oct. 2021, doi: 10.1109/JEDS.2021.3116975.

[35] M. Mehrpoo, F. Sebastiano, E. Charbon, and M. Babaie, "A cryogenic CMOS parametric amplifier," *IEEE Solid-State Circuits Lett.*, vol. 3, pp. 5–8, Oct. 2019, doi: 10.1109/LSSC.2019.2950186.

[36] B. Prabowo et al., "A cryo-CMOS receiver with 15 K noise temperature achieving 9.8dB SNR in 10 μs integration time for spin qubit readout," in *Proc. IEEE Int. Solid-State Circuits Conf.*, 2024, pp. 474–476, doi: 10.1109/ISSCC49657.2024.10454300.

[37] B. Prabowo, "Data underlying the publication: SNR in spin qubit gate-based readout and its impacts on readout electronics," 2023, doi: 10.4121/ad8cbe46-abd8-4d16-9672-18737177e096.

Bagas Prabowo (Student Member, IEEE) received the B.Sc. degree in electrical engineering from the University of Twente, Enschede, The Netherlands, in 2018, and the M.Sc. degree in electrical engineering in 2020 from the Delft University of Technology, Delft, The Netherlands, where he is currently working toward the Ph.D. degree in electrical engineering with QuTech.

His research interests include cryogenic RF integrated circuits for quantum computer applications with a focus on qubit readout, cryogenic electronics, cryogenic RF characterization, and wireless receivers.

Mr. Prabowo is a Reviewer for the IEEE SOLID-STATE CIRCUITS LETTERS (SSC-L).

Jurgen Dijkema received the B.Sc. degree (cum laude) in applied physics from the Hague University of Applied Sciences, Delft, The Netherlands, in 2017, and the M.Sc. degree in applied physics with an annotation quantum technologies in 2020 from the Delft University of Technology, Delft where he is currently working toward the Ph.D. degree, focusing on using superconducting resonators for long range coupling and rapid readout of spin qubits, with QuTech.

Xiao Xue received the B.S. degree in physics from the University of Science and Technology of China (USTC), Hefei, China, in 2014, and the Ph.D. degree (cum laude) in physics from the Delft University of Technology (TU Delft), Delft, The Netherlands, in 2022.

He is a Postdoc Researcher with QuTech, TU Delft. His key achievements include the first demonstration of high-fidelity two-qubit logic in silicon crossing the error correction threshold, the first universal control over spin qubits with a cryo-CMOS controller—"Horse Ridge," and the first long-distance two-qubit logic between spatially separated spin qubits in silicon. His research interests include quantum information processing with spin qubits in silicon quantum dots, benchmark and optimization of quantum logic, circuit quantum electrodynamics with spin qubits, and quantum control using cryogenic CMOS circuitry, and using on-chip superconducting resonators for rapid readout of spin qubits.

Dr. Xue was the recipient of the Steven Hoogendijk Prize in 2023 for his contributions. He is currently a Lead Investigator of a National Growth Fund—Quantum Technology 2023.

Fabio Sebastiano (Senior Member, IEEE) received the B.Sc. (cum laude) and M.Sc. (cum laude) degrees in electrical engineering from the University of Pisa, Pisa, Italy, in 2003 and 2005, respectively, the M.Sc. degree (cum laude) in engineering from the Sant–Anna School of Advanced Studies, Pisa, in 2006, and the Ph.D. degree from the Delft University of Technology, Delft, The Netherlands, in 2011.

From 2006 to 2013, he was with NXP Semiconductors Research, Eindhoven, The Netherlands, where he conducted research on fully integrated CMOS frequency references, nanometer temperature sensors, and area-efficient interfaces for magnetic sensors. In 2013, he joined the Delft University of Technology, where he is currently an Associate Professor. He has authored or coauthored one book, 11 patents, and more than 100 technical publications. His main research interests include cryogenic electronics, quantum computing, sensor read-outs, and fully integrated frequency references.

Dr. Sebastiano is on the Technical Program Committee of the ISSCC, and the IEEE RFIC Symposium, and has been on the program committee of IMS. He is currently an Associate Editor for IEEE TRANSACTIONS ON VERY LARGE SCALE INTEGRATION, IEEE JOURNAL OF SOLID-STATE CIRCUITS (JSSC), and was also a Guest Editor of the JSSC. He was the recipient of several awards, including the 2008 ISCAS Best Student Paper Award, 2017 DATE Best IP Award, ISSCC 2020 Jan van Vessem Award for Outstanding European Paper, and 2022 IEEE CICC Best Paper Award. He was a Distinguished Lecturer of the IEEE Solid-State Circuit Society.

Lieven M. K. Vandersypen received the M.Sc. degree in mechanical engineering from KU Leuven, Leuven, Belgium, in 1996, and the M.Sc. and Ph.D. degrees from Stanford University, Stanford, CA, USA, in 1997 and 2001, respectively. His Ph.D. research focused on quantum computing, making use of nuclear spins in molecules as quantum bits.

As a postdoctoral researcher, he then moved to Delft in 2001, where he established his own group in 2003, and pioneered the control and read-out of single-electron spins in semiconductor quantum dot arrays. With his QuTech colleagues, he currently focuses on scaling up spin qubits circuits, where exploratory physics goes hand in hand with high-level engineering. His research resulted in more than 165 publications that were cited more than 22 000 times. He is a Co-Founder and presently the Scientific Director of QuTech, and was the Co-Director of the Kavli Institute of Nanoscience. In 2015, his group started a close collaboration with Intel. His research resulted in more than 165 publications that were cited more than 22 000 times.

Dr. Vandersypen was a Member of the "The Young Academy" of the KNAW from 2007 to 2012. He is a Member of the Royal Holland Society of Sciences and Humanities and a Fellow of the American Physical Society. In 2010, he was a Visiting Scientist with the Massachusetts Institute of Technology, Cambridge, MA, USA. He was a Visiting Fellow with the University of New South Wales, Sydney, Australia, in 2015. He was a co-recipient of the IEEE ISSCC Jan Van Vessem Award for Outstanding European Paper in 2020, the Nicholas Kurti European Science Prize in 2008, the IUPAP Young Scientist Prize for Semiconductor Physics in 2008, and in 2021, the Spinoza Prize, the highest scientific distinction in The Netherlands.

Masoud Babaie (Senior Member, IEEE) received the B.Sc. degree (Hons.) in electrical engineering from the Amirkabir University of Technology, Tehran, Iran, in 2004, the M.Sc. degree in electrical engineering from the Sharif University of Technology, Tehran, in 2006, and the Ph.D. degree (cum laude) in electrical engineering from the Delft University of Technology, Delft, The Netherlands, in 2016.

From 2006 to 2011, he was with the Kavoshcom Research and Development Group, Tehran, where he was involved in designing wireless communication systems. From 2014 to 2015, he was a Visiting Scholar Researcher with the Berkeley Wireless Research Center, Berkeley, CA, USA. In 2016, he joined the Delft University of Technology, where he is currently an Associate Professor. He has authored or coauthored one book, three book chapters, 11 patents, and more than 100 peer-reviewed technical articles. His research interests include RF/millimeter-wave integrated circuits and systems for wireless communications and cryogenic electronics for quantum computation.

Dr. Babaie was the recipient of the 2015–2016 IEEE Solid-State Circuits Society Predoctoral Achievement Award, 2019 IEEE ISSCC Demonstration Session Certificate of Recognition, 2020 IEEE ISSCC Jan Van Vessem Award for Outstanding European Paper, 2022 IEEE CICC Best Paper Award, and 2023 IEEE IMS Best Student Paper Award (second place), and also Veni Award from the Netherlands Organization for Scientific Research in 2019. He is the Co-Chair of the Emerging Computing Devices and Circuits Subcommittee of the *IEEE European Solid-State Circuits Conference* (ESSCIRC) and the Technical Program Committee of the *IEEE International Solid-State Circuits Conference* (ISSCC). He is currently an Associate Editor for IEEE SOLID-STATE CIRCUITS LETTERS (SSC-L).